ELECTRONIC SUPPLEMENTARY INFORMATION FOR

Electronic Structure of Pyridine-based SAMs on Flat Au(111) Surfaces: Extended Charge Rearrangements and Fermi Level Pinning

ZhongYun Ma,[a] Ferdinand Rissner,[b] LinJun Wang,[a] Georg Heimel,[c] QiKai Li,[a]
Zhigang Shuai*[ad] and Egbert Zojer*[b]

[a] *Key Laboratory of Organic Solids, Beijing National Laboratory for Molecular Sciences (BNLMS), Institute of Chemistry, Chinese Academy of Sciences, 100190 Beijing, People's Republic of China.*
[b] *Institute of Solid State Physics, Graz University of Technology, Petersgasse 16, A-8010 Graz, Austria. E-mail: egbert.zojer@tugraz.at*
[c] *Insitut für Physik, Humboldt-Universität zu Berlin, Brook-Taylor-Strasse 6, 12489 Berlin, Germany*
[d] *Department of Chemistry, Tsinghua University, 100084 Beijing, People's Republic of China. E-mail: zgshuai@tsinghua.edu.cn*

1. Nature of the highest occupied states and the lowest unoccupied states of the isolated monolayers

In order to constitute a continuous transport channel through the SAM, states need to be delocalized spanning the whole region between the metal electrodes. Moreover, to consistently analyze the relation between certain states in different SAMs, their detailed character needs to be known. Therefore, we have analyzed the various peaks in the projected density of states (PDOS) of individual atoms and their sum, the density of states projected onto the molecular part (MDOS). For this analysis we have plotted the local density of states (LDOS) integrated in an energy window (±0.10 eV) around the respective PDOS peaks. The results are shown in Figure S1 and S2 here and Figure 4 in the main text. The main observations shall be briefly discussed in the following.

A common feature of the highest occupied state is that it displays σ-character and is localized in the vicinity of the N atom (see peak I of each 1-ring monolayer in Figure S1 and Figure S2). Only for $–NO_2$ containing SAMs, it also has significant contributions from the substituent. This state strongly hybridizes with the Au states upon bonding to the Au (111) surface, and then is no longer resolved as a separate peak (cf. main text and Ref. [1,2]).

Below the highest occupied σ-state, for all the 1-ring systems, there are two close-lying states with π-character. The π-state with significant density on the axial C-atoms (cf. peak II in Figure 4 of the main text) is referred to as type-(1), and the π-state where the axial C atoms are within a nodal plane (cf. the peak III in Figure 4 of the main text) is denoted as type-(2). For the $–NH_2$ substituent, the type-(1) state is higher in energy; however, the order of the states is reversed for the $–NO_2$, –H, $–CH_3$ and $–CF_3$ substituted systems, and for –CN (see the peak II in Figure S1(b)) they appear to overlap (there the peak III displays features of a σ-state on the backbone overlapping with a π-state on the substituent). For the SAMs with $–NH_2$, $–NO_2$, or

–CN substituents, where the π-system extends onto the substituent, the higher-lying π-state is also the one with the larger density on the substituent. For the $–NO_2$ substituted SAMs, an additional occupied state of σ-symmetry (peak II) localized at the tail group is found above the π-states.

For the longer oligophenylenes with $–NH_2$ substituent and the Pyr|3P|CN monolayer, the LDOSs of the highest occupied states shown in Figure S2 imply that the type-(1) π-state is destabilized and overlaps with the σ-state localized in the vicinity of the N-atom. For the $–NO_2$ substituted monolayers and the Pyr|2P|CN, the highest occupied state maintains the same character as in the 1-ring system, and the first π-states are found at lower energies.

Compared to the complications for the occupied states, the situation for the lowest unoccupied state in the studied systems is much more straightforward. It is always of π-character (see peak i of all the 1-ring monolayers in Figure S1). The situation is somewhat modified in Pyr|1P|NH_2 and Pyr|2P|NH_2 (cf., the discussions in the main manuscript and section (4) below). The density on the substituent associated with the lowest π-state is small for the –H, $–CH_3$, and $–CF_3$ substituted systems, it increases for the $–NH_2$ case, increases further for –CN and becomes a maximum for the $–NO_2$ substituent.

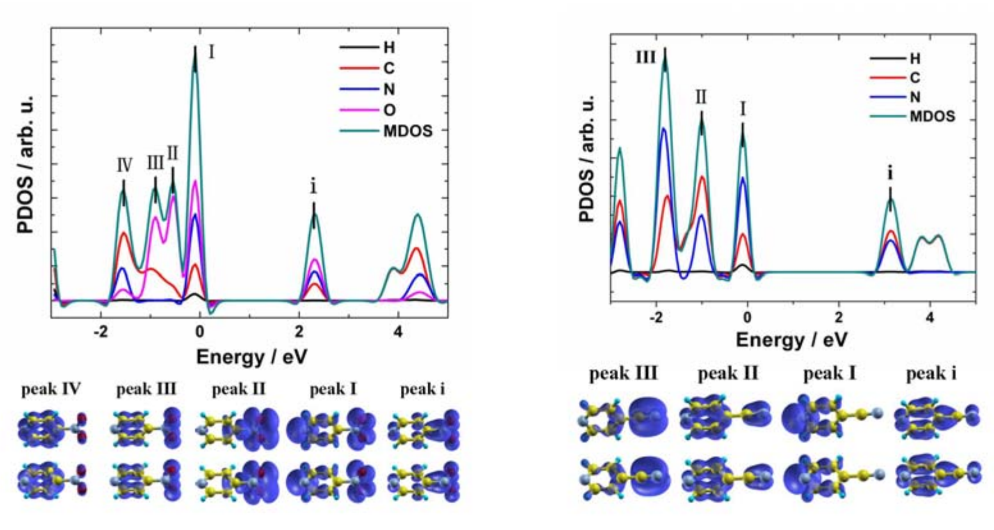

(a) Pyr|1P|NO_2

(b) Pyr|1P|CN

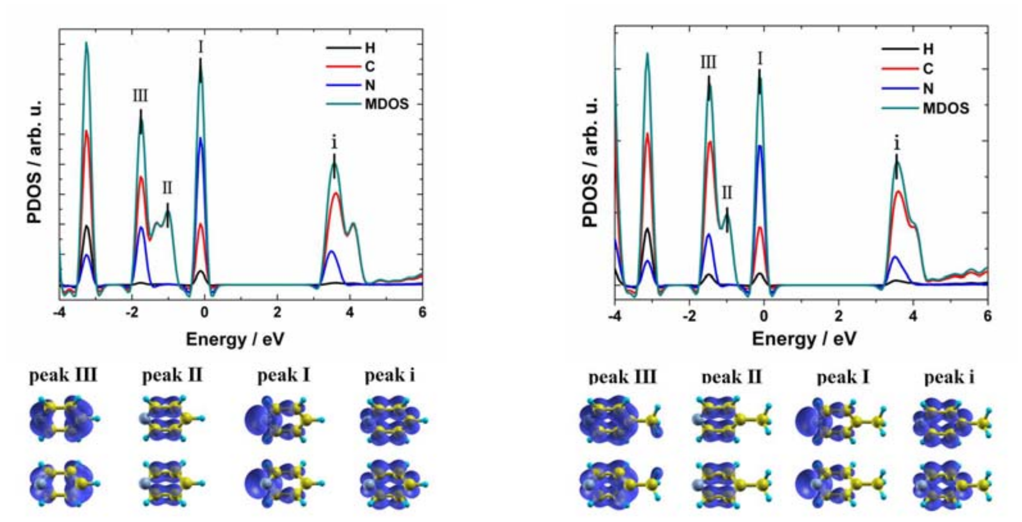

(c) Pyr|1P|H　　**(d) Pyr|1P|CH_3**

(e) Pyr|1P|CF_3

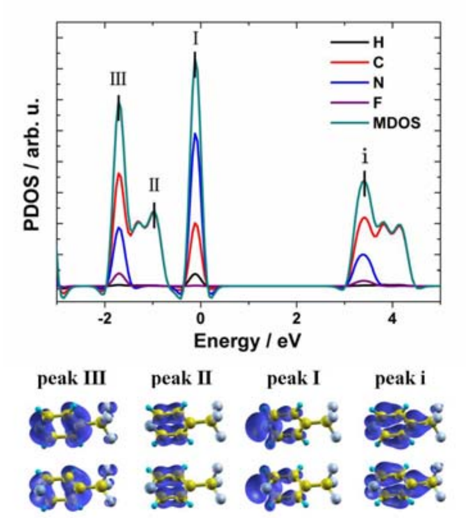

Figure S1. *Density of states projected onto hydrogen (H), carbon (C), nitrogen (N), oxygen (O) and fluorine (F) atoms in the Pyr|1P|X isolated monolayer (X = $-NO_2$, $-CN$, $-H$, $-CH_3$, $-CF_3$ from (a)-(e), respectively). The highest occupied peaks are denoted with I, II, III and IV, and the lowest unoccupied peak is denoted as i. The panels below the PDOS show the local density of states, LDOS, associated with these peaks for the two molecules within one unit cell. It has been obtained by integrating over an energy interval of ±0.10 eV around the peak positions.*

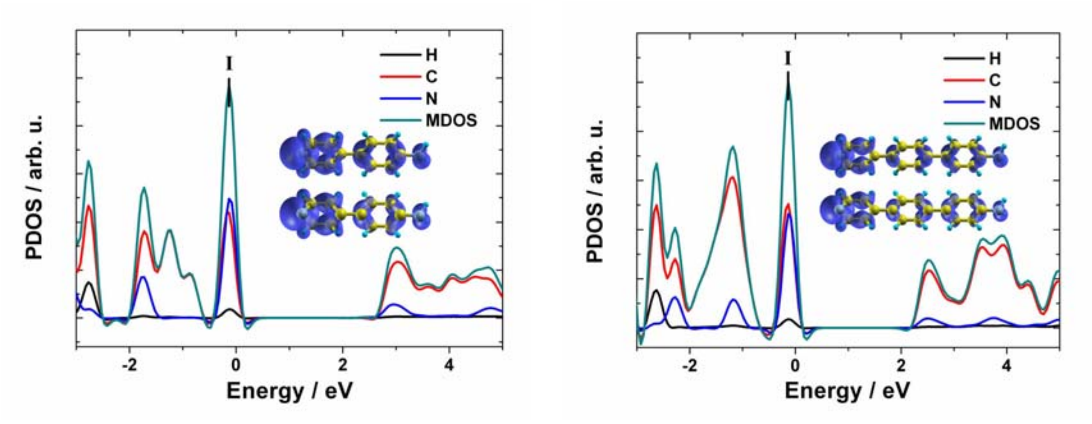
(a) Pyr|2P|NH$_2$ **(b) Pyr|3P|NH$_2$**

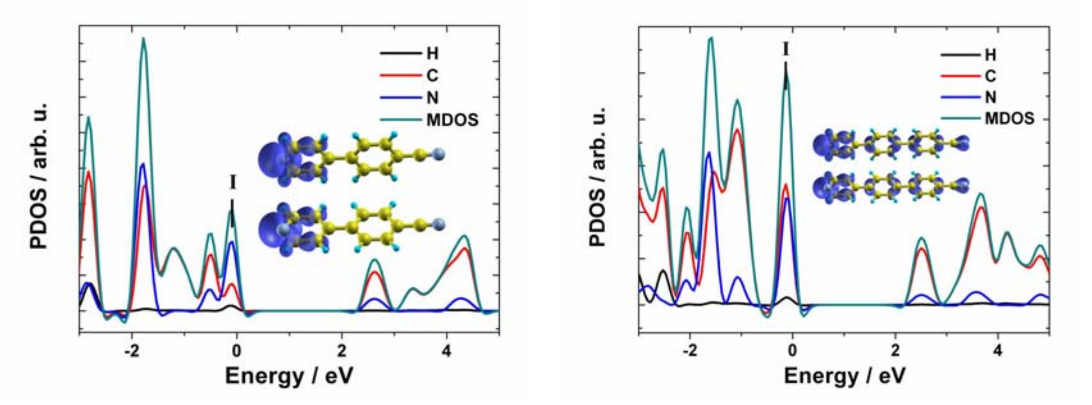
(c) Pyr|2P|CN **(d) Pyr|3P|CN**

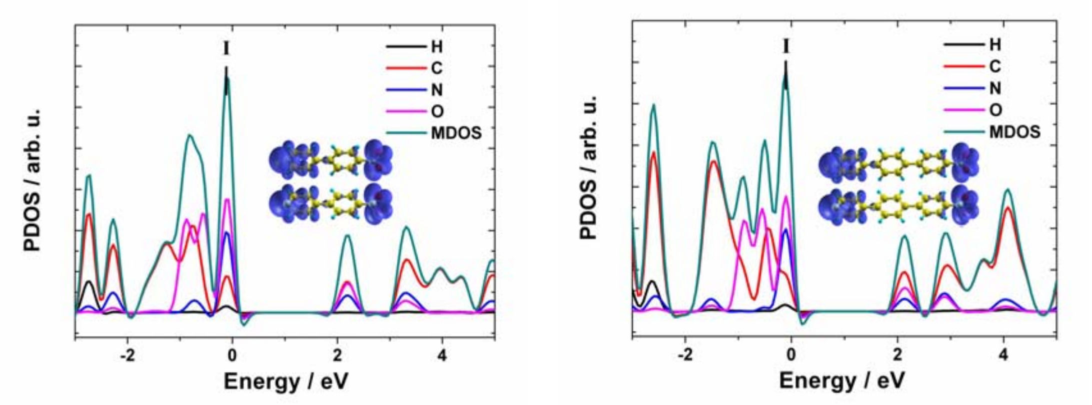
(e) Pyr|2P|NO$_2$ **(f) Pyr|3P|NO$_2$**

Figure S2. *Density of states projected onto hydrogen (H), carbon (C), nitrogen (N), oxygen (O) atoms in the isolated monolayers (X = –NH$_2$, –CN, –NO$_2$, from (a)-(f), respectively) for the two- and three-ring systems. Local densities of states, LDOS, associated with the highest occupied peaks (denoted by I) are shown in the insets. They have been obtained by integrating over an energy interval of ±0.10 eV around the peak positions.*

2. Nature of the highest occupied states and the lowest unoccupied states of the interacting SAM-metal systems

When the SAMs are bonded to the Au(111) surfaces via the pyridine group, the σ-state localized close to the nitrogen atom can no longer be resolved as a proper peak. Consequently, in all systems apart from the –NO_2 substituted SAMs, the first peak in the occupied PDOS corresponds to a delocalized π-state. In the latter, several peaks associated with occupied σ-states are found at higher energies. The highest occupied π-state (HOPS) is of type (2) for all 1-ring systems apart from the –NH_2 and –CN substituted ones. For the longer backbones, due to the increased conjugation, the HOPS are always type (1) and are well delocalized along the whole backbone.

(a)

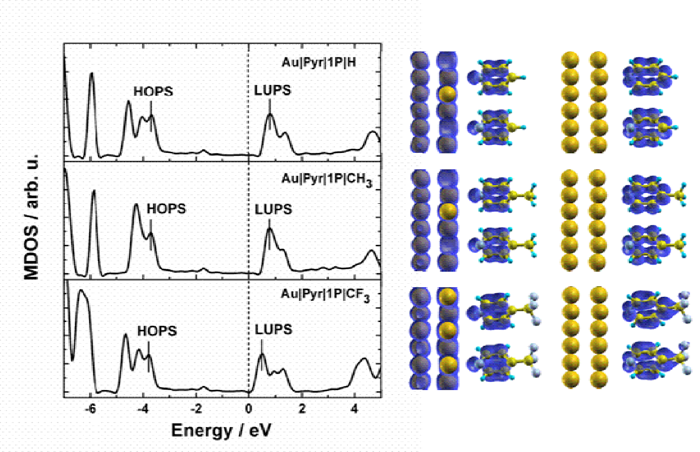

(b)

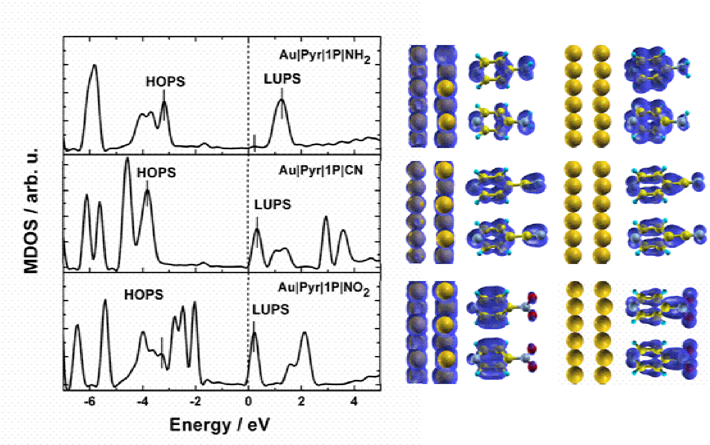

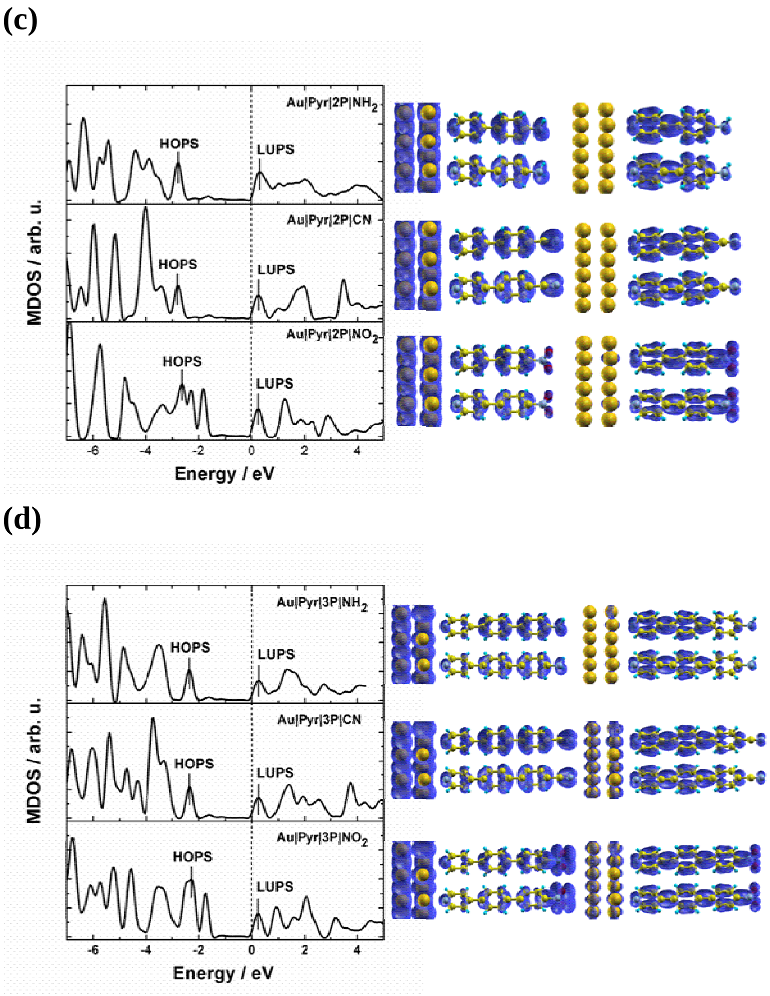

Figure S3. *Left: density of states projected onto the SAM part of the combined metal-SAM systems, MDOS, for the investigated 1-ring (a and b), 2-ring (c) and 3-ring (d) systems. The structures of the SAMs are given directly in the graphs using the naming convention adopted throughout the manuscript. Right: LDOSs associated with the highest occupied and lowest unoccupied π-state. They have been obtained by integrating over an energy interval of ±0.10 eV around the peak positions. Only the top two Au layers are shown.*

3. Charge carrier redistributions and resulting changes in the electrostatic energy associated with the metal-SAM bond formation for the –H, $-CH_3$, $-CF_3$ substituted systems

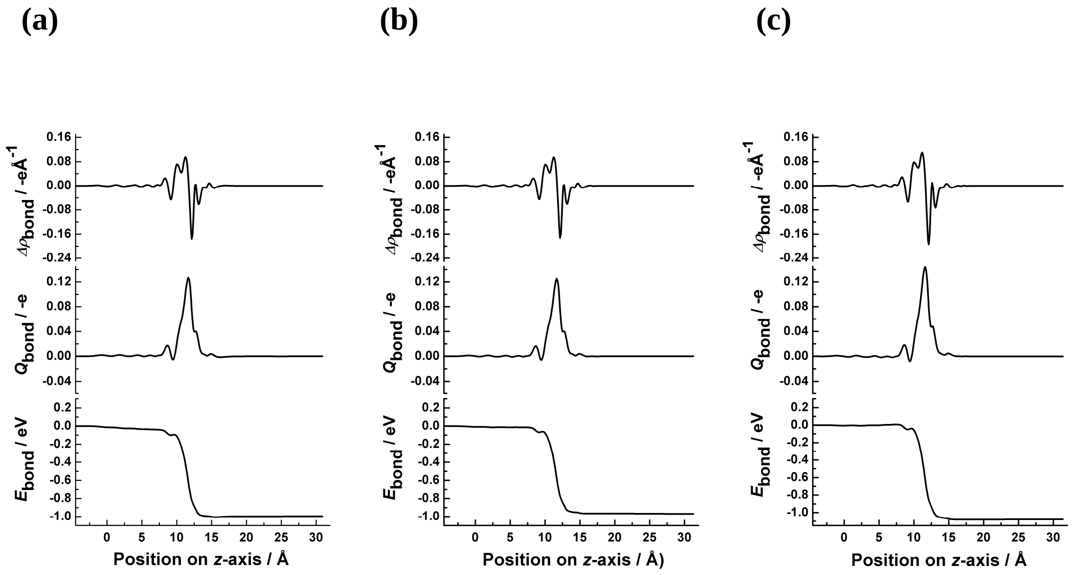

Figure S4. *Charge rearrangements upon bond formation (*$\Delta\rho_{bond}$*), net charge transfer (*$Q_{bond,}$*), as well as the resulting change in the electrostatic energy (*E_{bond}*) for Au|Pyr|1P|H (a), Au|Pyr|1P|*CH_3 *(b), and Au|Pyr|1P|*CF_3 *(c).*

4. Understanding the bonding-induced charge rearrangements in Au|Pyr|1P|NH_2 and Au|Pyr|2P|NH_2

As described in the main manuscript, there is a large contribution from the tail group region to $\Delta\rho_{\mathrm{bond}}$ (and thus Q_{bond} and E_{bond}) for Au|Pyr|1P|NH_2 and Au|Pyr|2P|NH_2, but not for any other system - including the closely related Au|Pyr|3P|NH_2. In order to study the origin of this peculiar shape of the $\Delta\rho_{\mathrm{bond}}$ curves, we show the detailed 3D plots for the regions with negative $\Delta\rho_{\mathrm{bond}}$ (electron depletion) and the regions with positive $\Delta\rho_{\mathrm{bond}}$ (electron accumulation) separately in Figure S5, using Au|Pyr|1P|NH_2 as an example. It can be seen that some electron density accumulates in a region above the –NH_2 groups. Still, although this accumulation is small (cf. small isodensity value used for producing that plot), it plays a significant role for the bond dipole in Au|Pyr|1P|NH_2 and Au|Pyr|2P|NH_2 (cf. Fig. 5a,b in the main text). In order to exclude that this surprising observation (i.e., charge shifting to relatively far from the actual atoms of the SAM) is merely a consequence of an inadequate methodology, we performed extensive tests addressing the reliability of our VASP calculations in this respect.

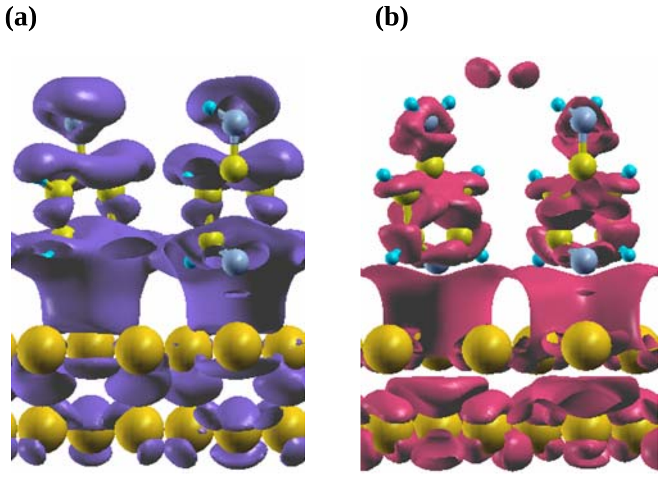

Figure S5. *3D Isodensity representation of* $\Delta\rho_{bond}$ *for a SAM of Pyr|1P|*NH_2 *on a 5-layer Au(111) slab (only the top two layers are shown), isovalue=0.00072 e/*$Å^3$. *Electrons flow from the electron-depletion region (a) to the electron-accumulating region (b).*

As a first check, we tested the impact of changing several of the key parameters in the VASP calculations. These include the cutoff energy for the plane wave basis (40 Ryd instead of 20 Ryd), the number of *k*-points, the smearing width and method, the type of pseudopotentials (hard instead of soft) and the *xc*-functional (PBE instead of PW91). It turned out that none of those measures qualitatively changed the charge rearrangements shown in Figure S5.

In order to further test the influence of the basis functions, we repeated the calculations on the systems Au|Pyr|1P|NH_2 and Au|Pyr|2P|NH_2 applying the linear combination of atomic orbitals (LCAO) code SIESTA.[3] I.e., in these calculations, instead of using a plane wave basis, atomic orbital type basis functions of double-zeta polarized (DZP) quality have been used. The same geometries as in the VASP calculations were used together with the PBE functional and the use of symmetric unit cells prevents spurious electrostatic interaction between neighboring slabs. Interestingly, the “unusual” charge rearrangements are completely absent in those calculations. This raises the important question which code provides a more accurate description of the bond-dipole for the short chain –NH_2 substituted SAMs. Also the origin of the observed discrepancies needs to be clarified.

Therefore, we compared the eigenvalue spectra obtained with both two codes for the *isolated* Pyr|2P|NH_2 molecule (in the same geometry it adopts in the SAM). In this comparison we also used a third software package, Turbomole 5.7.1,[4] because it allows to choose from a much larger variety of atomic-orbital based basis sets. In this way, we were able to obtain the eigenenergies using five different basis sets: a split-valence polarized basis (SVP) [5] and the augmented correlation-consistent basis sets aug-cc-PVDZ and aug-cc-PVTZ [6] in Turbomole, a double-zeta polarized basis (DZP) in SIESTA and plane waves in VASP. In all cases, we used the PBE functional except in the VASP calculations where PW91 is used (*vide supra*).

The obtained energies of the Kohn-Sham orbitals are shown in Figure S6. Except for the small basis set SVP, the eigenenergies between the different basis sets match very well for the occupied states; the small deviation of the plane-wave spectrum reflects the impact of the used functional. Clearly, the situation is more complex for the unoccupied orbitals. Here, one might argue that unoccupied Kohn-Sham orbitals are of limited meaning anyway, but one has to keep in mind that upon Fermi level pinning the lowest unoccupied band actually becomes partially occupied without changing its nature (see main manuscript). Therefore, looking at the unoccupied states in the non-bonded molecules and layers is of some significance in the present case.

Although the overall correspondence between the VASP (plane-wave) and the SIESTA (DZP) calculation is not too bad, there are also certain differences. Most importantly, the state marked as “L+3”, i.e. LUMO+3, in the plane-wave spectrum seems to be missing when using DZP. A closer look at the real-space representation of those orbitals (given in Fig. S6b for each basis set) reveals that this is not the case: this orbital is found to be the “L+4” with DZP and at about 1.5 eV above its

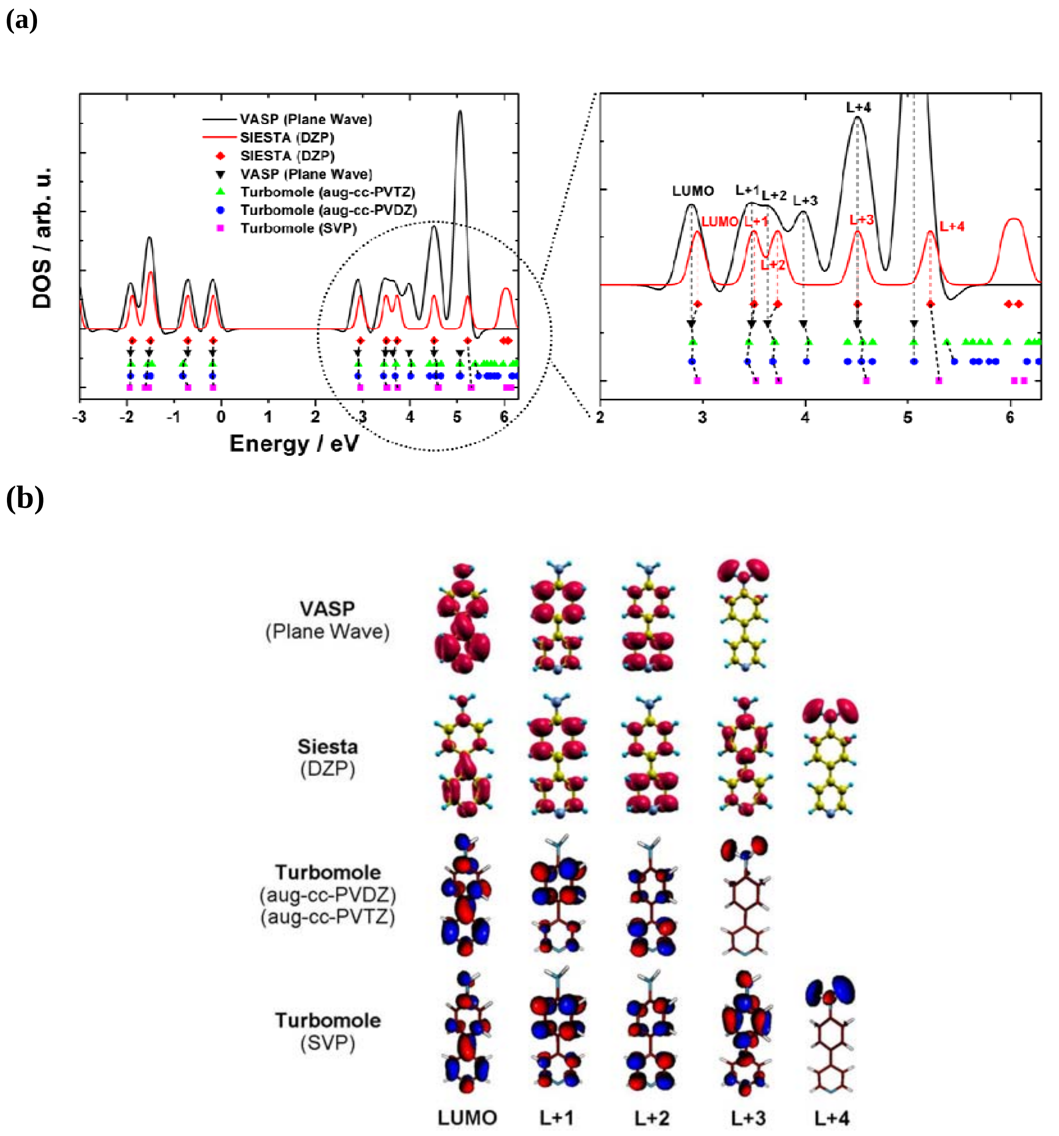

Figure S6. *(a) top: DOS of the isolated Pyr|2P|*NH_2 *molecule obtained from DFT calculations employing VASP and SIESTA codes with different basis sets; bottom: corresponding eigenvalues from the VASP, SIESTA, and Turbomole calculations (indicated by different symbols). For the sake of clarity, a zoom in is shown for the unoccupied states. The equivalent eigenvalues (in the energy interval from -2 to 5.5 eV) are connected by the dashed lines as a guide to the eye. The zero points in the horizontal axis represent the onset of the HOMO peak. (b) 3D representation of the unoccupied states as obtained in the various calculations.*

plane-wave equivalent. Such a result can be interpreted in the context of MacDonald's theorem,[7] according to which the eigenvalues obtained using a certain incomplete basis set are upper limits and approach the correct values as the basis set approaches completeness. Although the chosen basis sets do not approach completeness in any systematic way, it can be easily observed that the eigenvalues are shifted down with increasing basis set quality. This already strongly indicates the superiority of the plane-wave calculations over DZP and such an interpretation is further backed up by the presented Turbomole calculations. While the Turbomole SVP eigenvalues are reminiscent of the SIESTA DZP results, both aug-cc basis sets nicely reproduce the VASP plane-wave spectrum.

This “problematic” unoccupied orbital (i.e., the LUMO+3 in the VASP calculations of the isolated molecule) turns out to be the key to understand the peculiar charge rearrangements in Au|Pyr|1P|NH_2 and Au|Pyr|2P|NH_2. Starting from the molecular eigenspectrum it is possible to understand the electronic structure of SAMs formed from those molecules and consequently the charge rearrangements upon adsorption.

To avoid unneeded complexity, we continue the discussion for the one-ring system. Figure S7a and b compare the DOS of molecule and monolayer of the Pyr|1P|NH_2 molecules along with the corresponding real-space representations. Besides the obvious similarities, there is an important difference: The molecular LUMO does *not* constitute the lowest unoccupied band in the monolayer. Instead, a very broad band originating from the molecular LUMO+1 is found as the valence band. This is a consequence of the electrostatic landscape in such a SAM, cf. Fig. 2b in the main text. An orbital localized at the very “right” end of the Pyr|xP|NH_2 SAM is shifted down in energy way more than an orbital delocalized over a large part of the molecule such as the LUMO. This way, the molecular L+1 is shifted to below the LUMO in the monolayer. As contact to the metal is established and Fermi-level pinning occurs, it thus, becomes involved in the pinning process (see Fig. S7c). This is also nicely illustrated by a comparison of the 3D isodensity representation (Fig. S7c) and the corresponding onset of the valence band (Fig. S7b).

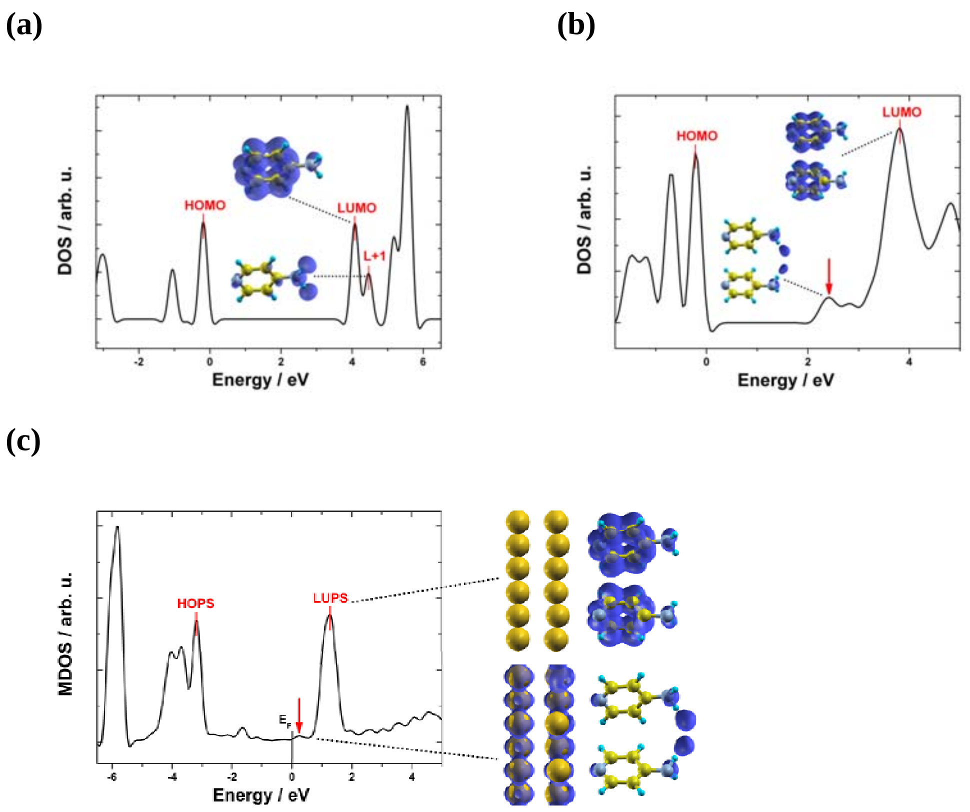

Figure S7. *The density of states (DOS) of the Pyr|1P|NH$_2$ molecule, (a), the isolated monolayer, (b, not including Au substrate), and the combined system Au|Pyr|1P|NH$_2$, (c). The zero points in the horizontal axis represent the onset of the HOMO peak in the isolated systems (a, b) and the Fermi level in the combined system (c), respectively. The insets shows the LDOS plots for the LUMO/LUPS and the localized tail-group states ("L+1" state in (a) and the states that the arrows point to in (b) and (c), which we attribute to the low energy part of a dispersing band originating from what is originally the LUMO+1).*

Having discussed those peculiarities, it is now also possible to explain their absence in the very similar system Au|Pyr|3P|NH$_2$. Because the length of the conjugated backbone is increased from 1P to 3P, the energy gap decreases, causing the π-conjugated LUMO to shift downwards. Correspondingly, the energetic distance between LUMO and the localized state responsible for the discussed charge rearrangements increases in the isolated molecule. Although the latter state shifts down in energy in the molecule-to-monolayer transition in each system, it does not cross the LUMO anymore for the 3P backbone. This is illustrated in Fig. S8, which shows the energetic distance between both involved states in the molecular and SAM configuration for all three backbone lengths.

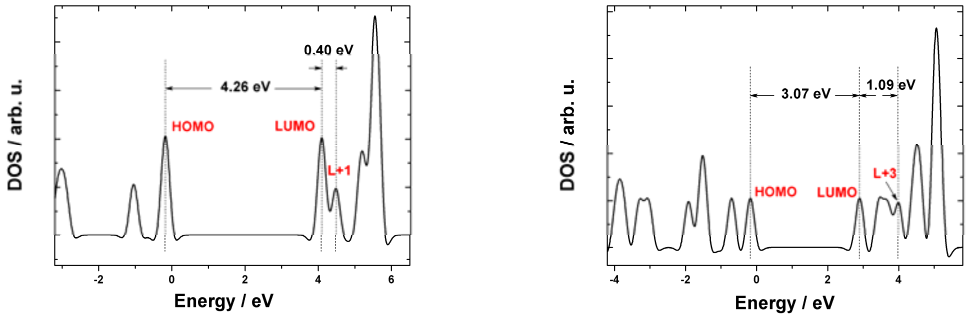

(a) Pyr|1P|NH$_2$

(b) Pyr|2P|NH$_2$

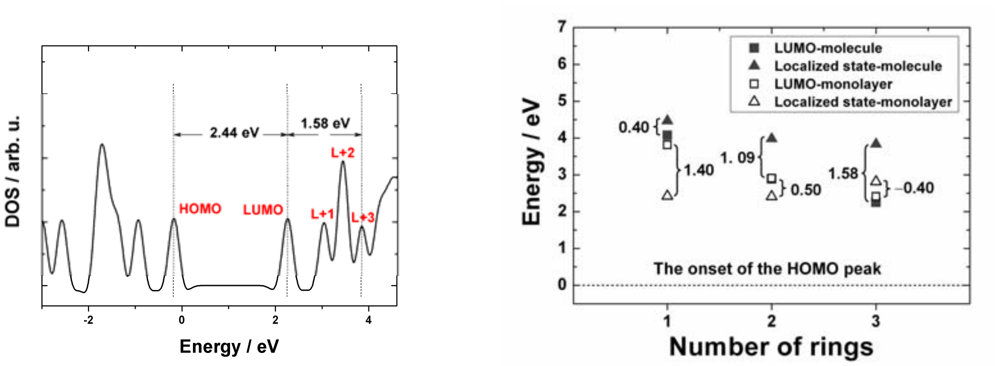

(c) Pyr|3P|NH$_2$

(d)

Figure S8. *DOS and energy gaps between the LUMO and the HOMO, state localized at the –NH$_2$ group for 1-,(a), 2-,(b), and 3-ring (c) –NH$_2$ substituted molecules. The zero points in the horizontal axis represent the onset of the HOMO peaks. Panel (d) compares the chain-length dependence of the energetic positions of the LUMO (square) and the localized states (triangles) for the Pyr|nP|NH$_2$ (n=1, 2, 3) isolated molecules (filled symbols) and monolayers (open symbols). The energies are given relative to the onset of the HOMO.*

5. Test calculations using hybrid functionals

We also performed test calculations using the HSE06 functional [8,9] on two representative SAMs, namely Pyr|1P|H and Pyr|1P|NH_2 layers in the absence of the metallic substrate using the VASP 5.2.11 code. The single-point calculations were based on the PW91 geometries. The energy cutoff, *k*-mesh, and other settings were left unaltered compared to the PW91 simulations. Preconverged PBE orbitals were used as starting guesses in the HSE calculations.

The calculated densities of states (DOS) are shown in Figure S9. For the sake of convenience, the corresponding DOS from the PW91 calculations are also provided. The actual shape of the DOS changes, but the order of the bands does not, albeit the splitting between features I and II is reduced in the HSE calculations. For Pyr|1P|NH_2 they actually overlap as for the Pyr|2P|NH_2 and Pyr|3P|NH_2 free-standing SAMs when using the PW91 functional (see Table 2 in the manuscript and Figure S2(a) and (b)).

As expected, the HSE calculations also increase the gap. The π-LUMO is shifted up by 1.78 eV in Pyr|1P|H and by 1.66 eV Pyr|1P|NH_2 relative to the onset of the HOMO peak. Considering a typical bond dipole of -1 eV in the absence of significant pinning, this leaves Pyr|1P|H in a non-pinned situation as for the PW91 functional, while Pyr|1P|NH_2 with an EA^{dock} of 4.14 eV will be found right at the onset of pinning. Keeping in mind that the HSE gap at the surface is presumably overestimated as a consequence of the incorrect description of screening above the metal surface, this indicates that Pyr|1P|NH_2 is pinned as already obtained by PW91. Also in longer chains, in which the band-gap is further reduced pinning can be expected to prevail. The higher LUMO energy for the HSE calculations will, however, result in the necessary charge rearrangements decreasing in magnitude.

Moreover, the unusual feature (i) due to the –NH_2 substituent shown in Fig. 4 of the manuscript and discussed in detail in section 4 of this ESI is present also in the HSE calculated DOS of Pyr|1P|NH_2; I.e., it can be expected to play a significant role for the pinning-induced charge rearrangements also when using hybrid functionals.

(a) Pyr|1P|H (PW91) (b) Pyr|1P|H (HSE06)

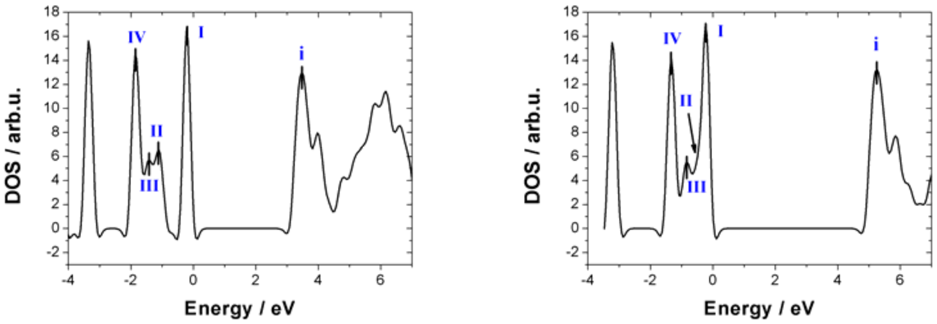

(c) Pyr|1P|NH_2 (PW91) (d) Pyr|1P|NH_2 (HSE06)

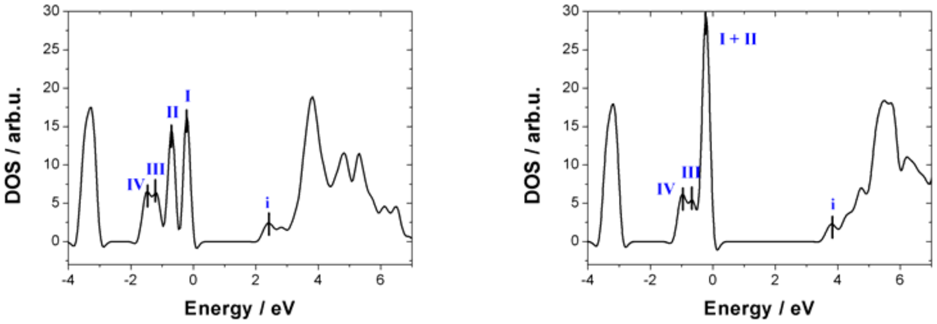

Figure S9. *The density of states (DOS) of the two free-standing SAMs, Pyr|1P|H and Pyr|1P|NH_2, calculated using the HSE06 functionals and the PW91 functionals. The highest occupied peaks are denoted with I, II, III and IV, and the lowest unoccupied peak is denoted as i. The energy axis is aligned at the onset of the HOMO peak.*

References

(1) A. Bilić, J. R. Reimers and N. S. Hush, *J. Phys. Chem. B*, 2002, **106**, 6740.
(2) S. Hou, J. Ning, Z. Shen, X. Zhao and Z. Xue, *Chem. Phys.*, 2006, **327**, 1-9.
(3) J. M. Soler, E. Artacho, J. D. Gale, A. Garcia, J. Junquera, P. Ordejon and D. Sanchez-Portal, *J. Phys.: Condens. Matter*, 2002, **14**, 2745.
(4) R. Ahlrichs, M.Baer, M. Haeser, H. Horn and C. Koelmel, *Chem. Phys. Lett.* 1989, **162**, 165; O. Treutler and R. Ahlrichs, *J. Chem. Phys.* 1995, **102**, 346; F. Furche and R.Ahlrichs, *J. Chem. Phys.* 2002, **117**, 7433.
(5) A. Schäfer, H. Horn and R. Ahlrichs, *J. Chem. Phys.,* 1992, **97**, 2571.
(6) D. E. Woon and T. H. Dunning Jr, *J. Chem. Phys.,* 1993, **98**, 1358.
(7) J. K. L. MacDonald, *Phys. Rev.* 1933, **43**, 830.
(8) J. Heyd, J. E. Peralta, G. E. Scuseria, and R. L. Martin, *J. Chem. Phys.*, 2005, **123**, 174101.
(9) J. Heyd, G. E. Scuseria, and M. Ernzerhof, *J. Chem. Phys.*, 2006, **124**, 219906.